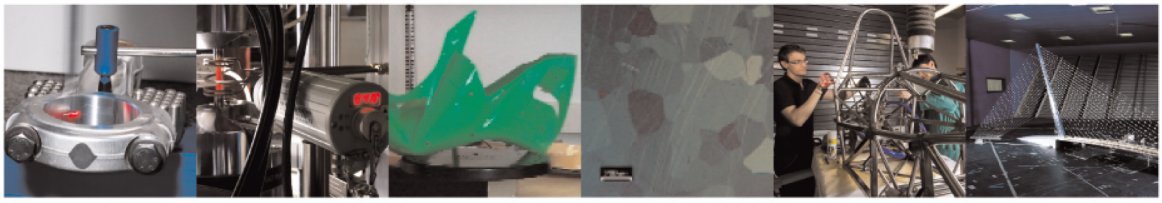

Estimating crack tip position in adhesively bonded joints subjected to mode II quasi-static loading

M. Mehrabi, L.M. Martulli, A. Bernasconi, M. Carboni

This is a post-peer-review, pre-copyedit version of an article published in Fatigue and Fracture of Engineering Materials and Structures. The final authenticated version is available online at: http://dx.doi.org/doi:10.1111/ffe.14237

DIPARTIMENTO DI MECCANICA ■ POLITECNICO DI MILANO
via G. La Masa, 1 ■ 20156 Milano ■ EMAIL (PEC): pecmecc@cert.polimi.it
http://www.mecc.polimi.it
Rev. 0

Estimating crack tip position in adhesively bonded joints subjected to mode II quasi-static loading

M. Mehrabi [1], L.M. Martulli [1], A. Bernasconi [1], M. Carboni [1]*

[1] Dept. Mechanical Engineering, Politecnico di Milano, Milano, Italy

Abstract

This study aimed at estimating crack tip position in adhesive bonded joints under mode II quasi-static loading using experimental and numerical approaches. Experimental techniques were utilized and compared, including optical backscatter reflectometry, visual testing and a novel strategy based on digital image correlation. Additionally, a finite element analysis was employed to identify the numerical crack tip position and the extent of damage within the bondline. This analysis revealed that a significant portion of the crack propagation region in the adhesive is occupied by the fracture process zone. Moreover, optical backscatter reflectometry shows the potential to detect this process zone within the adhesive that the other methods may not detect. This capability is particularly beneficial for detecting damage at early stages.

Keywords: Adhesive bonded joints; Crack tip position; Quasi-static mode II loading; Optical backscatter reflectometry; Digital image correlation; Fracture process zone.

[*] Corresponding author:

E-mail address: michele.carboni@polimi.it (M. Carboni).

1 Introduction

Adhesive bonding is one of the most known and adopted joining methods, receiving attention, for example, in aerospace and automotive industries where reliability, strength, fatigue resistance, and lightness of joints are required simultaneously [1,2].

These joints are frequently subjected to a combination of different loading modes, such as mode I and mode II. Mode I loading (opening mode) applies a tensile stress normal to the crack plane, causing the crack faces to move directly apart. Mode II loading (in-plane shearing) applies a shear stress parallel to the crack plane and perpendicular to the crack front, causing the crack faces to slide relatively to each other. Mode I loading has received significant attention from researchers [3-6], as it is the most common and detrimental loading mode. However, studies [7,8] have shown that mode II loading can also significantly contribute to joint failure. Therefore, mode II loading must be also understood and accounted for developing robust adhesive bonding systems.

One of the major challenges associated with adhesive bonded joints is to guarantee the in-service structural integrity of the joints over time. To address this challenge, Structural Health Monitoring (SHM) and Non-Destructive Testing (NDT) are often employed [9]. Techniques such as Visual Testing (VT) [10,11], penetrant testing [12,13], ultrasonic guided waves [14], acoustic emission [15], X-ray computed tomography [9,16], and ultrasonic microscopy [9] have been used for the inspection and characterization of cracks in adhesive joints under mode II loading. Among these techniques, VT is one of the most common, rapid, and intuitive techniques for monitoring crack propagation and it is the only standardized technique [9]. It has proven to be effective in mode I loading [3,17,18]. In mode II loading, however, the crack does not often propagate straight and smooth as in mode I loading [9,11]. On top of that, the absence of crack opening makes it challenging to detect the crack tip accurately. These factors can affect the accuracy of measurements and introduce uncertainties [10,11].

Experimental strain measuring techniques are also useful for crack monitoring of adhesive joints. One such technique is Digital Image Correlation (DIC), providing valuable information about strain distribution in joints. This method has been used successfully to locate and quantify cracks in adhesive joints under mode I loading [3,4,18,19], but requires further research for mode II loading [13,20]. Optical fibres are another practical method that provides strain measurement for crack monitoring in adhesive joints. The

most common fibre optic systems are Fibre Bragg Gratings (FBG) [21,22], Chirped FBG (CFBG) [23], and Optical Backscatter Reflectometry (OBR) [24]. Unlike FBG and CFBG, OBR offers distributed strain sensing over long distances. It employs swept wavelength interferometry to measure changes in the optical fibre's refractive index. This allows for high-resolution strain sensing over varying lengths [24]. In contrast to DIC, OBR is more ideal for in-service damage monitoring due its precision, compactness and ease of calibration [18]. Analogous to DIC, the applicability of the OBR for crack monitoring in adhesively bonded joints under mode II loading is still an ongoing area of research [12].

While experimental methods can provide valuable insights into the crack behavior of adhesive joints, they can be supported by the numerical interpretation. The Finite Element (FE) modelling is a useful numerical approach to study the crack propagation and damage behavior within the bondline under mode II loading. Cohesive Zone Modelling (CZM) is a popular approach in FE modelling of bonded surfaces, that combines continuum and fracture mechanics to simulate damage initiation and propagation [25]. Compared to conventional methods in fracture mechanics, the CZM technique is less sensitive to mesh configuration and does not require an initial defect [26]. The effectiveness of CZM largely depends on the type of Traction-Separation Laws (TSLs). TSLs describe the constitutive relationships between the interfacial tractions and the corresponding displacement jumps of the nodes of a cohesive element as it undergoes deformation. Different types of TSLs have been proposed in the literature [27], such as exponential, bi-linear, or trapezoidal. The choice of a TSL is generally based on the specific material properties and loading conditions. For instance, bi-linear TSLs are suitable for brittle adhesives [28], while trapezoidal TSLs are preferred for ductile adhesives [29]. This is because ductile materials typically undergo significant plastic deformation before failure, which can be better represented by a trapezoidal TSL [28,29]. Taking advantage of CZM, some studies [25,30,31] have successfully analysed crack propagation in adhesive joints under mode II loading [25,27,32,33].

The main objective of this study is to investigate the crack length estimation in metal-to-metal End-Notched Flexure (ENF) bonded joints subjected to quasi-static mode II loading. The study employs both experimental and numerical methods to monitor the crack initiation and propagation. To this end, the OBR's back-face strain measurement and a novel DIC-based strategy are used as the experimental methods. These methods are then compared to VT and another DIC-based method developed by Orell et al. [13].

Additionally, FE analysis is used to improve the interpretation of the experimental results by providing numerical crack tip location and the extent of damage within the bondline. Cohesive properties for modelling the adhesive layer in FEM were derived through numerical optimization. The combination of experimental and numerical analysis allows for a thorough comparison of crack tip position estimation using various monitoring approaches.

2 Experimental procedures

2.1 Materials and ENF sample fabrication

The adopted adhesive is a bi-component epoxy 3M Scotch-weld^{TM} 7260B/A Non-sag, and the substrate is a high strength DIN 40CrMoMn7 steel grade. The mechanical properties of the materials were taken from the experimental work of [25], tabulated in Table 1. The sample dimensions followed the ASTM D3433 standard and are schematically depicted in Fig. 1.

Table 1. Mechanical properties of adhesive and adherend [25]. "±" denotes standard deviation.

Material	Young's modulus [MPa]	Yield stress [MPa]	Ultimate stress [MPa]	Poisson's Ratio
Adhesive 3M Scotch-Weld™ 7260B/A	4,248 ± 297	35 ± 2	40.6 ± 1.5	0.35
Adherend steel DIN 40CrMoMn7	205,000	861	1,000	0.29

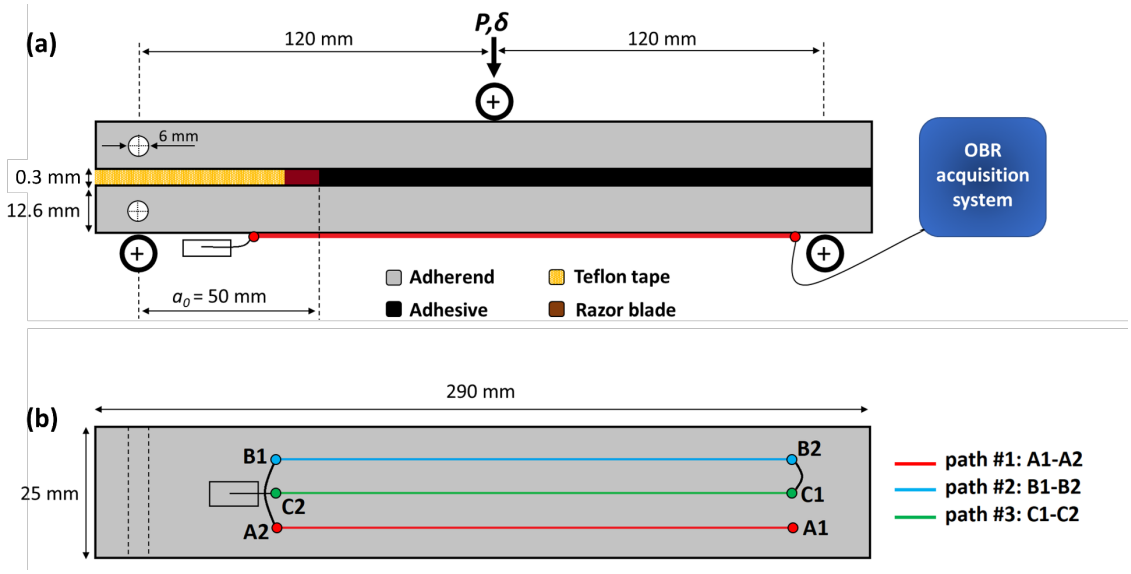

Fig. 1. Three-point bending ENF test configuration: (a) side view of the sample while optical fibre (red line) bonded to the bottom surface of the adherend, (b) bottom view of the sample showing parallel paths of optical fibre bonded to the back-face of the adherend (not scale drawing).

Manufacturing of the samples began by sandblasting the adherends. After sandblasting, the surface of the adherends were thoroughly cleaned with acetone. To guarantee the uniformity of 0.3 mm adhesive thickness over the bondline, glass microspheres with diameter of about 0.3 mm were mixed with the adhesive. The weight ratio of the glass microspheres to the adhesive is 2%. In addition, a 0.15 mm thick Teflon tape was bonded to inner part of the upper and lower adherends (total thickness of 0.3 mm) to prevent bonding and create an initial notch of 50 mm. The use of Teflon also minimized the friction between the adherends during the test. To create a sharp initial notch tip, a razor blade was inserted at the beginning of the adhesive bondline.

The adhesive curing process was completed in an oven through the following stages: a 1.5-hour increasing ramp from room temperature to 65 °C, followed by a 3-hour period of continuous temperature at 65 °C, and lastly a 1-hour decreasing ramp from 65 °C to room temperature. Afterwards, the overflown adhesive was cleaned from the lateral surfaces of ENF samples. Two specimens, named S1 and S2, were manufactured using the described procedure. Before performing the ENF test, the blade was taken out from the sample S1 to check its influence on the structural behaviour with respect to the case of specimen S2 where the blade was left in place.

2.2 Crack monitoring setup and measurement procedure

2.2.1 End-notched flexure test configuration

The three-point bending ENF test was chosen for the experimental quasi-static tests (see Fig. 1(a)). The MTS Alliance RF/150 electro-mechanical testing system was employed with a 150 kN load cell. The test speed rate was 0.8 mm/min. The load (P) and displacement (δ) of the testing machine were acquired throughout each test.

2.2.2 Visual testing

An Allied Vision Manta CCD camera equipped with an Optem lens system mounted on the back side of the specimen was used to track the crack propagation by the VT method (see Fig. 2 (a)). To increase the contrast between the lateral surface of the specimen and the crack, a water-based white paint was uniformly applied to the background surface. A high frame rate video (120 frame/second) was captured by the visual camera during each test and the magnification was set to 1.1x. The footage was then converted into individual image frames using MATLAB®. Corresponding values of load and crosshead displacement, acquired by the testing machine, were then associated to each frame for data analysis.

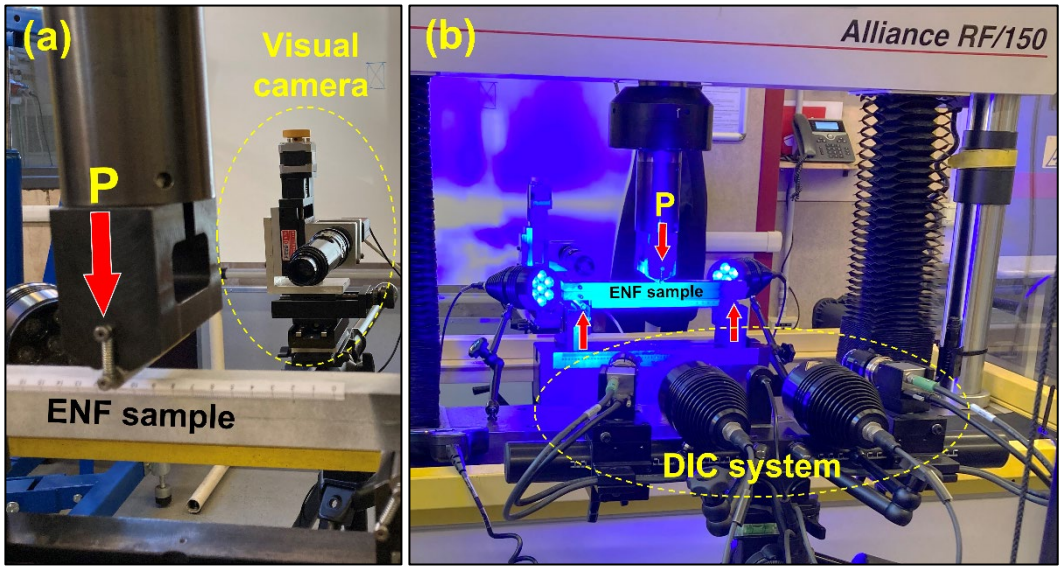

Fig. 2. Three-point bending ENF test setup: (a) The visual camera mounted on the back side of the ENF specimen and (b) DIC device mounted on the front side of the ENF specimen.

2.2.3 Digital image correlation

A stochastic and high-contrast (black and white) speckle pattern was painted on the lateral surface of the ENF samples to be used with DIC. The speckle pattern was created as follows: a base layer of water-based white paint was first applied. Then, black paint was randomly sprayed from varying distances and angles to create the random speckle pattern. The DIC system utilized in this study was the 3D measuring instrument GOM ARAMIS equipped with 12 megapixels cameras, while GOM Correlate software (ver. 2020) served as the post-processing software. The system was mounted on the lateral side of ENF samples to measure the strain field (see Fig. 2 (b)). The acquisition frequency was then set to 2 Hz, and, for the region of interest, subset size and step size were adjusted to 33 and 11 pixels, respectively.

2.2.4 Optical backscatter reflectometry

Following the layout in Fig. 1, optical fibres were bonded to the bottom surface of adherend using the HBM X60 bicomponent epoxy adhesive. As shown in Fig. 1, three parallel paths of optical fibres were adopted for strain measurement to detect any non-straight crack front. Prior to bonding, the surface was thoroughly cleaned. The 2 meters long optical fibre was connected to an OBR interrogator (ODiSI-B by OBR Luna Innovations Inc.) via an LC/APC connector. The OBR interrogator captures the Rayleigh backscattering pattern throughout the fibre and, by means of a suitable calibration, converts it to strain values. The device was connected to a PC for data processing, visualization, and storage purposes. The data acquisition frequency was set to 5 Hz. Furthermore, the length of virtual strain gauges over the fibre-optic was 1.3 mm with adjacent sensors being superimposed by 0.65 mm. Additionally, a taring procedure was considered before data acquisition during tests.

3 Numerical modelling

FE analysis was performed using ABAQUS/Standard 2018 (Dassault Systèmes Simulia Corp.) on the ENF sample under mode II loading to support the interpretation of the estimated position detected by VT, OBR and DIC. For the simulation of the crack propagation within the adhesive layer, the Cohesive Zone Model (CZM) [25] was used considering both a bi-linear and a trapezoidal Traction-Separation Law (TSL), as depicted

in Fig. 3. While a bi-linear TSL is commonly associated to brittle adhesives and the a trapezoidal one to ductile ones, in some researches [25,34,35] the bi-linear TSL was successfully employed to model ductile adhesives. To explore this further, both triangular and trapezoidal models were used for the ductile adhesive considered in this study.

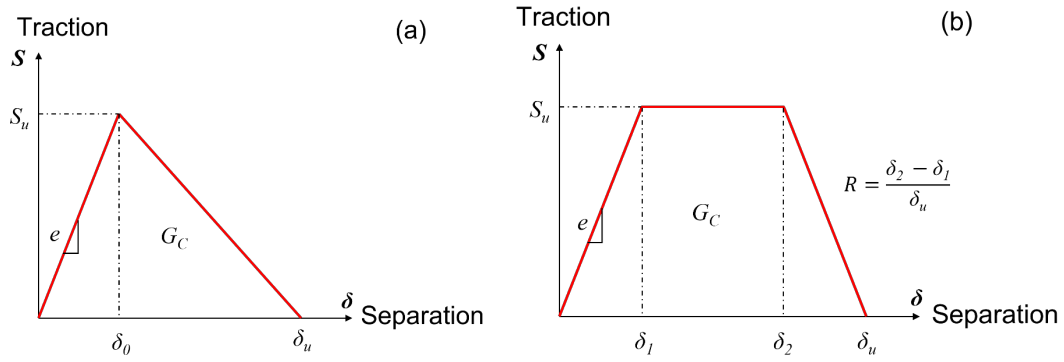

Fig. 3. (a) Bi-linear and (b) trapezoidal traction-separation laws.

3.1 FE model of ENF test

The specimen geometry of the 2D FE model follows Fig. 1. Following the experiments, the Teflon tape was modelled between the two adherends alongside of the notch to correctly simulate their sliding during the test. For simplicity and computational efficiency, the adherends and adhesive were modelled as a solid part, and then partitioned suitably. A friction coefficient of 0.01 was considered to model the contact between the Teflon layers, while a value of 0.2 was used to model the contact between the adherends and roller surfaces.

Three reference points (red points in Fig. 4) were defined at the centre of each roller, coupled to the external circumferences of their corresponding rollers. To simulate the displacement-controlled test, a vertical displacement of 3.2 mm was applied to the reference point of the upper roller. This specific displacement value was derived from the experimental load-displacement curve when the test was interrupted (see Section 4.1). Additionally, all displacements and rotations of the support rollers were constrained.

The mesh size for the adherend and the adhesive is 1×1 mm and 1×0.3 mm, respectively. Besides, four-node bi-linear plane-stress quadrilateral 2D solid elements were considered for the adherends using reduced integration (CPS4R). For the adhesive layer, four-node linear 2D cohesive elements (COH2D4) were employed. To ensure

comparability with reference [25], the plane-stress condition was applied in this study.[25] Moreover, a comparison between the plane-stress and plane-strain conditions revealed only a negligible difference in the results.

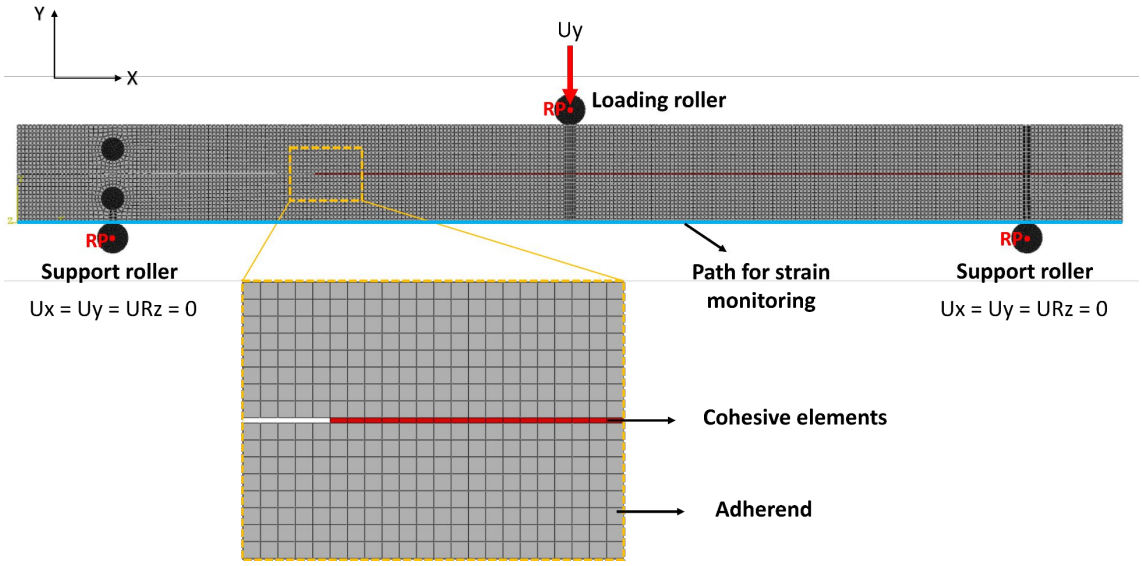

Fig. 4. FEM model of ENF sample.

The material properties of the adhesive and the adherends are based on Table 1. Three primary parameters namely the critical strain energy release rate (G_C), the initial stiffness parameter (e), and the ultimate stress (S) are required for the implementation of CZM according to the bi-linear TSL. Moreover, the R ratio ($R = \frac{\delta_2 - \delta_1}{\delta_u}$) must also be considered for the trapezoidal TSL. Note that the bi-linear TSL is a specific trapezoidal TSL with $R=0$. The estimation of the parameters is described in the following sub-sections.

3.2 Estimation of input parameters

3.2.1 Critical strain energy release rate (G_{IIC})

Three well-known analytical approaches are introduced to estimate the mode II critical toughness (G_{IIC}) from the experiments: the Compliance Calibration Method (CCM), the Compliance-Based Beam Method (CBBM) and the J-integral method.

The Compliance Calibration Method (CCM) developed by Wang and Williams [36], combines the Irwin-Kies's equation and the Corrected Beam Theory. The CCM assumes that the compliance of the specimen, which is the ratio of the displacement to the load (P/δ), is a function of the crack length (a). Note that the VT measurement was used for

determining the crack length.

$$G_{IIC} = \frac{3mP^2a^2}{2b}, \quad (1)$$

where b is the width of the adherend, and m is a coefficient derived by the regression analysis between specimen compliance ($C = \delta/P$) and the cubic crack length (a^3):

$$C = D + ma^3, \quad (2)$$

and D is a constant value.

De Moura and de Morais [37] developed a method called Compliance-Based Beam Method (CBBM) that utilizes beam theory and specimen compliance during testing. Using CBBM, the mode II critical toughness (G_{IIC}) can be estimated without measuring the crack length during the ENF test:

$$G_{IIC} = \frac{9P^2a_e^2}{16b^2E_fh^3}, \quad (3)$$

where h is the thickness of the adherend. a_e stands for the equivalent crack length that considers the effect of the FPZ, which is calculated by:

$$a_e = \left[\frac{C_{corr}}{C_{0corr}}a_0^3 + \frac{2}{3}\left(\frac{C_{corr}}{C_{0corr}} - 1\right)L^3\right]^{\frac{1}{3}}, \quad (4)$$

where L is the span length and a_0 is the notch length, whereas C_{corr} is the corrected compliance expressed as:

$$C_{corr} = C - \frac{3L}{10Gbh}, \quad (5)$$

The C_{0corr} is initial corrected compliance, following the same formula in Equation (5), and the G stands for shear modulus of the adherend. The E_f in Equation (3) is the flexural modulus of the specimen, considering the effect of the adhesive presence:

$$E_f = \frac{3a_0^3+2L^3}{8bh^3C_{0corr}}, \quad (6)$$

The J-integral method developed by Rice [38] is a contour integral that is independent of path and its value can be interpreted as the energy release rate under damage formation.

Therefore, it can be an alternative to accurately estimate the G_{IIC} when the Linear Elastic Fracture Mechanics (LEFM) assumption is invalid, particularly in the analysis of adhesives working into the plastic regime.

Taking advantage of the strain of the adherend and adhesive, Leffler [39] presented a simpler formulation of the J-integral to derive mode II critical toughness, eliminating the need for rotation calculations:

$$J \approx \frac{9(Pa_0)^2}{16b^2Eh^3} + \frac{3Pv_0}{8bh}, \qquad (7)$$

where a_0 is notch length, E is Young's modulus of the adherend, and v_0 is local sliding at the notch tip, which is measured using DIC at each acquisition stage in this study (detail of which is addressed in [39]). A comparison of the mode II critical toughness estimated by CCM, CBBM and J-integral method is shown in Table 2.

Table 2. Comparison of G_{IIC} values of the adhesive estimated by CCM, CBBM and J-integral methods for samples S1 and S2 and their mean values.

Samples	S1	S2	mean S1 - S2	Reference [25]
G_{IIC} by CBBM [N/mm]	10.8	10.56	10.68	6.63
G_{IIC} by J-integral [N/mm]	8.36	7.64	8	-
G_{IIC} by CCM [N/mm]	7.3	5.23	6.27	-

As is evident in Table 2, the CBBM yields the highest G_{IIC} estimation among the three methods. Interestingly, it estimates larger G_{IIC} values compared to the findings reported in reference [25] for the same adhesive. This difference can be attributed to the absence of a pre-cracking stage in the current study, a stage that was utilized in [25]. As reported in [25], the pre-cracking procedure introduces a new length to the initial notch (a_0), which reduces the overall stiffness of the bonded joint, making it more compliant. The change in compliance directly impacts the final G_{IIC} values because the CBBM estimates it based on the actual compliance of the structure. It is worth noting that larger G_{IIC} values imply that more energy is required to propagate a crack, which leads to a larger area under the load-displacement curve. Consequently, this may result in a higher ultimate load and a delay in the initiation of crack propagation.

On the other hand, CCM shows the lowest G_{IIC} estimation compared to the other methods. One possible reason is that the CBBM takes into consideration the FPZ effect when calculating the equivalent crack length. This consideration can lead to a longer crack length, and consequently, a larger G_{IIC} estimation. Similarly, the J-integral method incorporates the non-linearity of the adhesive into its calculations, which is particularly useful for the ductile behavior of the considered adhesive in this work, leading to a higher estimation of G_{IIC}.

The use of the equivalent crack length (a_e) concept in CBBM eliminates the need for direct crack length measurement. However, a mismatch between the equivalent crack length and the measured one has been reported [40-42], affecting the estimated value of G_{IIC} negatively. On top of that, CBBM and CCM were established based on the linear elastic fracture mechanics (LEFM) that do not account for the ductile behaviour of the adhesive used in this research [33]. As a result, for the FE analysis, the mean G_{IIC} value estimated by the J-integral approach is here adopted.

3.2.2 Initial stiffness (e) and ultimate stress (S)

In order to determine the remaining CZM parameters i.e., initial stiffness (e_I and e_{II}) and ultimate stress (S_I and S_{II}), numerical optimizations were performed using the commercial software package Isight™ (ver. 6.3) developed by Dassault Systèmes Simulia Corp. as introduced by Cardamone et al. [25]. To this end, load-displacement curves of the FEM and experiments are matched by optimizing the CZM parameters through an iterative process.

The adopted objective function of the optimization is the sum of the squared difference between the load values of FEM and experiment for the same displacement, based on the Equation (7):

$$f = \sum_{i=1}^{n} \left(P_i^{exp} - P_i^{FEM} \right)^2 , \tag{7}$$

where n represents the number of sampling points, P_i^{exp} and P_i^{FEM} stand for the load values of the experiments and FEM, respectively. Furthermore, the Hooke-Jeeves direct method was selected for the optimization strategy. A thorough description of the optimization strategy in this study is provided in [33]. For mode I loading, the stiffness parameter is

defined as $e_I = E/t_a$, whereas for mode II loading, it is $e_{II} = G/t_a$. The t_a stands for the adhesive thickness, while E and G refer to the elastic and shear modulus of the bulk adhesive, respectively. This provides an approximate initial value of the stiffness parameter for the first iteration of optimization, offering a sufficiently high value to ensure convergence and prevents numerical issues. In some research [43,44], the value of the stiffness parameter was chosen significantly larger than the actual stiffness of the material (e.g., 10^6 or 10^7 MPa/mm). However, during the optimization, the value will be adjusted if the problem achieves convergence. Thus, initial and optimized values may differ. Indeed, the stiffness parameter, as noted in [45], lacks physical meaning. It does, however, have a significant numerical role in reproducing the observed experimental behaviour. It should be emphasized that for both bi-linear and trapezoidal TSLs, the critical fracture toughness G_C must be considered as a fixed input value, while optimization is performed just on stiffness (e) and ultimate stress (S).

4 Results and discussions

4.1 Load-displacement curve

Fig. 5 depicts the load-displacement curves for both S1 and S2 specimens in black circles. The load-displacement behaviour for both samples is consistent with the results reported in [25]. A comparison of the initial slope (from 0 to point A) and the fracture load (at point B) between the two curves reveals a negligible difference, which could be attributed to experimental uncertainties and sample manufacturing. This suggests that the presence of the blade in S1 has no significant effect on the compliance of S1. According to Fig. 5, three regions can be observed in the load-displacement curves, which is consistent with the observation described in [12]:

- 0 to A: the region with a steeper slope (higher stiffness), where the Fracture Process Zone (FPZ) is likely not to have yet formed.
- A to B: the region at which the slope of the curve decreases (compliance increases) and the FPZ is likely to be developing.
- B to C: the region at which the crack propagates unstably until it reaches the loading point. After point C, the crack is in its closest position to the loading point and there is insufficient driving force to propagate it further.

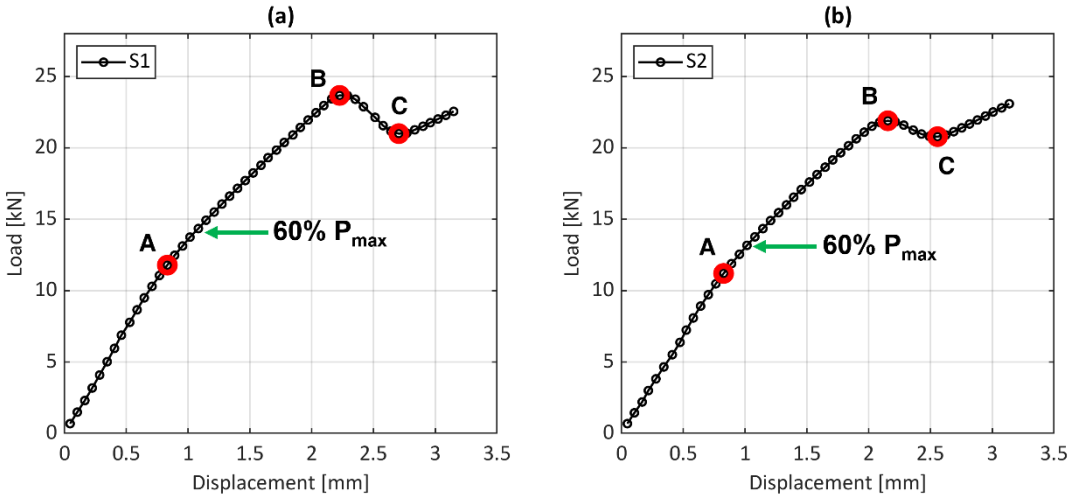

Fig. 5. ENF load-displacement curves of (a) S1 and (b) S2 represented three different regions: 0 to A: region with a steeper slope (higher stiffness), A to B: region where the compliance increases and the FPZ develops, and B to C: unstable crack propagation.

4.2 Methods for crack length estimation

4.2.1 Visual testing

According to the VT method, the crack tip was the point where the painting layer starts to fracture, as indicated by the black arrow in Fig. 6 (a). Subsequently, the assumed crack length was visually measured at each load level during the ENF test for S1 and S2, as shown in Fig. 6 (b). Additionally, three points on the load-displacement curve from Fig. 5 (points A, B, and C) are also marked in this figure.

Fig. 6 (a) reveals the non-uniformity of the crack growth under quasi-static mode II loading, which poses challenges in localizing the crack tip. For example, in the region from A to B in Fig. 6 (b), the crack tip identified by VT seems to advance by 12 mm and 10 mm in S1 and S2 specimens, respectively. Nevertheless, this region corresponds to the stage before unstable propagation occurs, where the FPZ is developing.

Furthermore, the measured length from 0 to A does not experience any visible change in both S1 and S2, showing that the FPZ is possibly has not yet formed. Finally, in the region from B to C, the unstable crack propagation measured by VT amounts to 38 mm and 37 mm for S1 and S2, respectively.

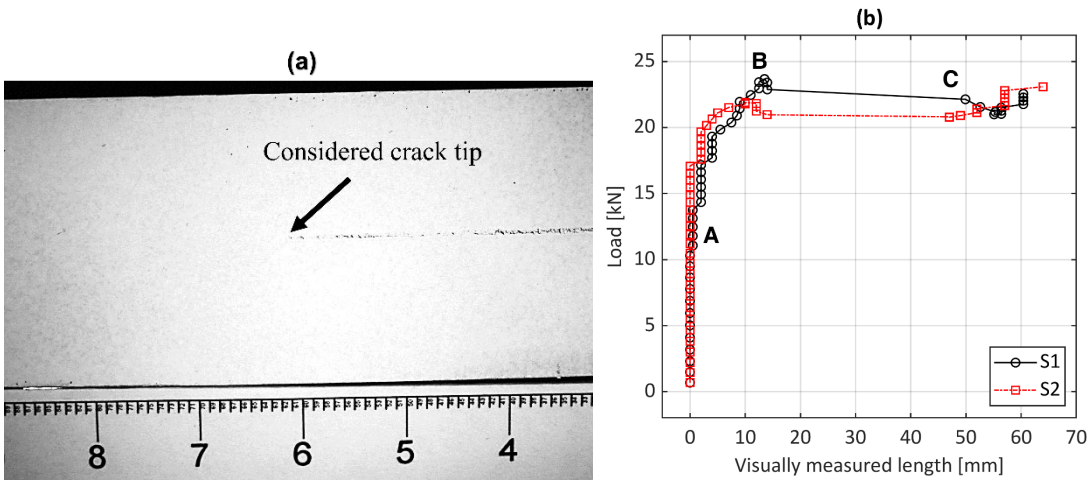

Fig. 6. Visual inspection for crack growth monitoring: (a) a frame captured by the visual camera for S1 (b) estimated crack length vs. load for S1 and S2 samples.

4.2.2 Digital image correlation

Considering the three-point bending ENF test, the shear deformation is mainly affecting the adhesive layer as its elastic modulus is significantly less than that of the steel adherends. This results in the adhesive layer experiencing higher strain values during the test. Therefore, analysing the shear strain directly along the adhesive layer may provide a useful feature for estimating the crack length. To this end, an acquisition line is applied over the adhesive bondline to directly extract the shear strain using GOM Correlate software (see Fig. 7(a)). In the software, the shear strain component on the x-y plane is denoted as "Epsilon (XY)". The measurement points along the acquisition line are spaced at intervals of 0.05 mm.

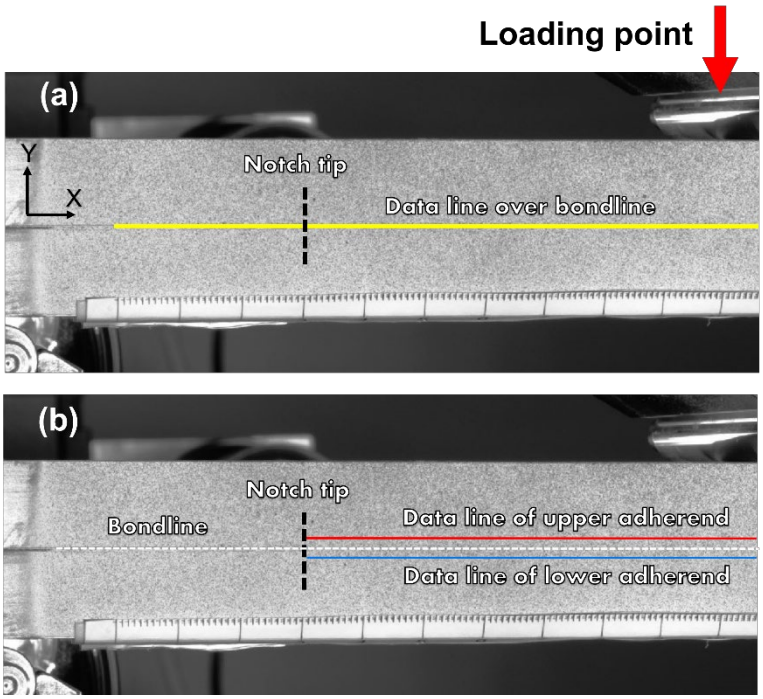

Fig. 7. Side view of the S1 sample captured by DIC (a) the data acquisition line over the adhesive bondline to directly extract the shear strain and (b) the data acquisition lines to measure the displacement of the upper and lower adherends.

The strain distribution along the data acquisition line in Fig. 7(a) was found to be separated into two regions: a fluctuating (noisy) region and a more steady one (see Fig. 8). This discrepancy in strain behaviour is likely due to the difference in strain morphology between the bonded and unbonded (fractured) regions. In the bonded area, the strain is relatively uniform and continuous, and there are no sudden changes in the geometry or material properties over the bondline. Therefore, the strain measurement obtained from DIC is more accurate, and there is less noise in the strain profile.

However, in the fractured region, there are large strain gradients due to the presence of the crack. In this region, friction between the two fracture surfaces, and their roughness, can also contribute to the noise in the strain profile. Therefore, the strain measurement in this region is more susceptible to noise. The separation between fluctuating and steady regions thus represents a transition point that can be inferred as the potential position of the crack tip.

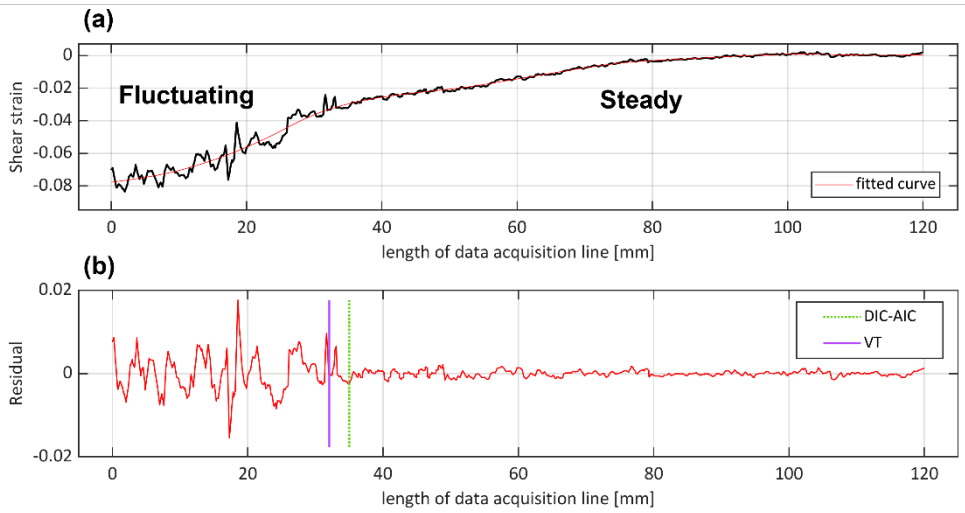

Fig. 8. (a) Fitting of the shear strain profile along the bondline under 16.6 kN load for S1 sample. (b) Residuals analysis for the identification of the transition point between the fluctuating and steady regions using AIC algorithm.

To better highlight the transition between the two regions, a nonlinear regression based on the smoothing spline algorithm was applied to the shear strain profile using MATLAB® (see Fig. 8(a)). This algorithm generates a cubic spline by minimizing a cost function that consists of the sum of the squared differences between the observed data and the fitted curve. To control the level of smoothness applied to the curve, the algorithm employs an associated Smoothing Parameter (SP), which is defined between 0 and 1. As SP approaches 1, the fitting curve closely fits the data points, whereas 0 provides the smoothest possible curve (a straight-line). In this study, the SP was set to 5e-3, which is small enough to effectively highlight the difference between the two regions. The residuals of such a regression were then extracted to facilitate the selection of the transition point between the two regions (see Fig. 8(b)).

The accurate estimation of the transition point between two regions is crucial for the proposed methodology. To address this challenge, an algorithm based on the Akaike Information Criterion (AIC) [46] is employed. AIC is frequently used in signal processing analysis [47], splitting the signal into two adjacent time series with distinct statistical characterizations. The separation point of the time series is distinguished by the point where the AIC is minimized. In this study, instead of time series, the shear strain with two distinct regions is introduced. In Fig. 8(b), the green dashed line (DIC-AIC) indicates the estimated transition point by AIC algorithm between the fluctuating and steady regions, as compared to the crack tip estimated by VT (purple line).

To evaluate the accuracy of the DIC-AIC technique, a comparison is made with another DIC-based method called Separated Adherend Zone (SAZ) introduced by Orell et al. [13]. The SAZ method analyses the strain in the adhesive layer indirectly by measuring the relative displacement of both the upper and lower adherends near the adhesive layer. To accomplish this, two data lines are defined at an equal distance (1.5 mm in this study) from the adhesive layer, as shown in Fig. 7(b). The objective is to measure the difference in the relative displacement of adherends, both horizontally (shear) and vertically (opening), at the initial notch tip when 60% of the maximum load is applied (near point A in Fig. 5). Then, the equivalent difference value is found for loads greater than 60%. Selecting 60% from the range of 50%, 60%, and 70% ensures a balance: it is sufficiently high to induce significant damage in the adhesive joint, yet low enough to ensure stable crack propagation that can be effectively monitored. This particular value aligns closely with point A, where the slope of the load-displacement curve changes, indicating the initiation of damage and carrying significant physical meaning (see Fig. 5). For further detailed information on this technique, readers may refer to [13].

Using the AIC algorithm in comparison to the SAZ approach, the crack length is derived at different stages of DIC, corresponding to the data points of load-displacement during the test, as shown in Fig. 9. For the sake of brevity, in this study, the SAZ method based on the horizontal and vertical relative displacements are referred to as DIC-SAZ-dX and DIC-SAZ-dY, respectively. The results show that there is a discrepancy between DIC-AIC and VT even at the initial load level, ranging from 0 to A. In fact, the DIC-AIC estimated a larger crack length, where it is expected to observe a length equal to the initial notch length (a_0). This overestimation implies that the transition point from the fluctuating region to the steady one may not be precisely located at the actual crack tip, but rather at a different location. In contrast, the DIC-SAZ method does not exhibit such an error. This is because it assumes that there is no crack initiation or propagation before the load reaches 60%, as shown in Fig. 9.

As the load increases from A to B, a discrepancy between both DIC methods and VT becomes evident. From point B onward, where the crack starts to propagate in an unstable manner, there is agreement between DIC-based techniques and VT in estimating the crack length. These observations suggest that both DIC-based approaches consistently estimate the initiation of the crack earlier than VT from point A to B, while during unstable propagation, there is good conformity between them. As the crack gets closer to the

loading point, the force that drives its propagation gradually decreases, which is why similar predictions are expected when approaching the loading point.

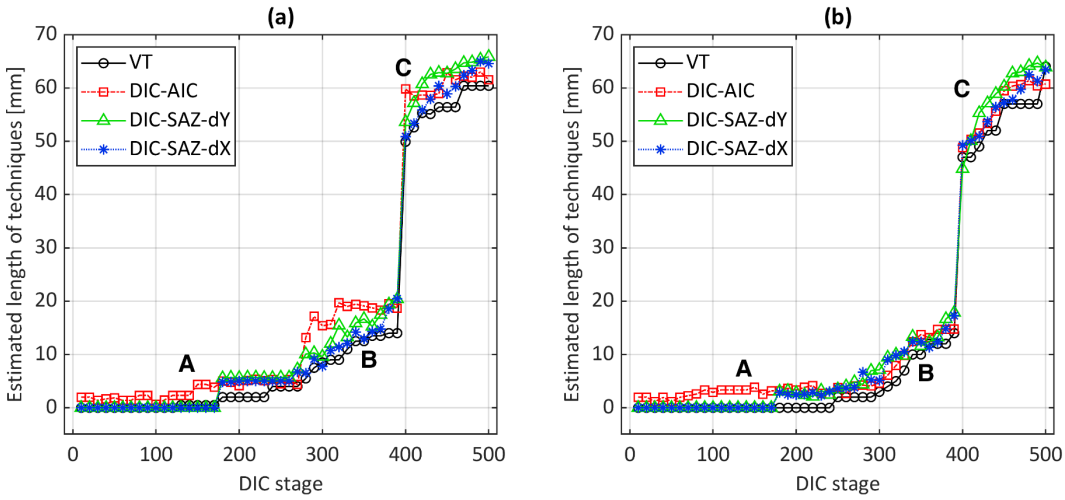

Fig. 9. Estimated crack length of experimental techniques at different stages of DIC using VT and DIC-based techniques for specimens (a) S1 and (b) S2.

4.2.3 Optical backscatter reflectometry

The variation of the strain distribution at the back-face of the ENF sample S1, measured with the OBR technique, is shown in Fig. 10. Each curve is associated with the strain distribution at a certain load level during the test, which is highlighted by different colours. Fig. 10 also demonstrates that there is a conformity between the three fibre paths A1-A2, B1-B2, and C1-C2 (see Fig. 1). Therefore, just the middle path (C1-C2) is considered for the following analysis. Some fluctuating behaviour can be observed in a few parts of the curves. This might be due to a lack of uniformity in the bonding of the fibre to the adherend since the fluctuating regions exhibit a similar trend as the load increases. Furthermore, since the OBR results for the S1 and S2 samples are nearly identical, the focus in this section will be on sample S2.

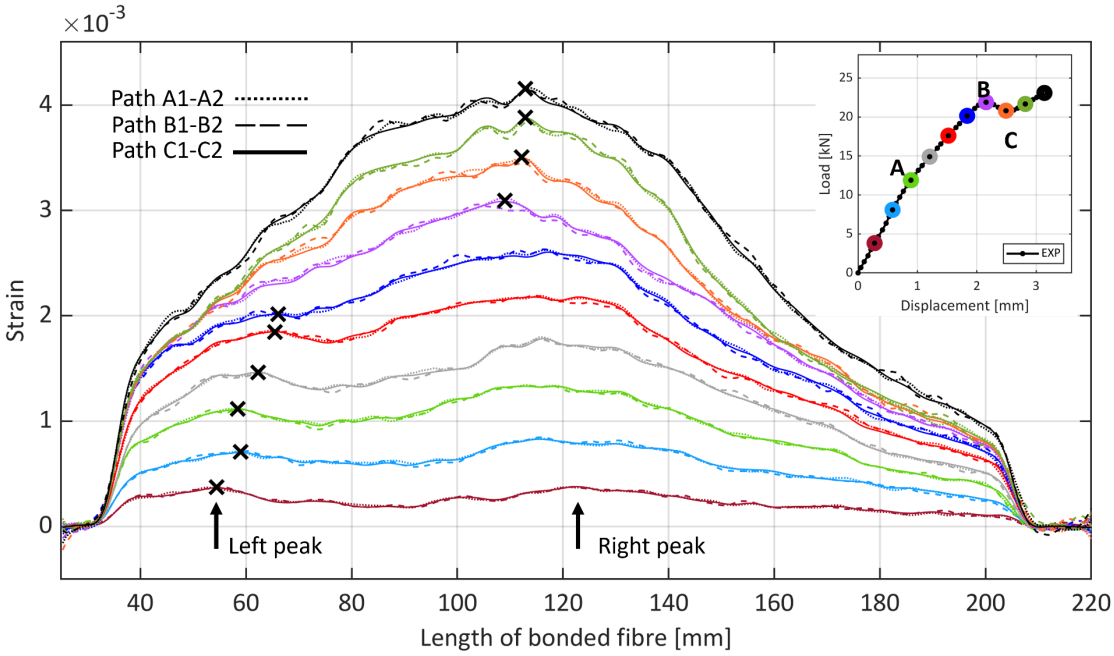

Fig. 10. Strain distribution of three optical fibre paths bonded to the adherend surface of S2 sample under different load levels.

According to Fig. 10, the strain profile shows two distinct peaks in the first region of the load-displacement curve, from 0 to A. The presence of the left peaks could be related to the transition from a more compliant structure (the two separated arms) to a less compliant structure (the bonded arms). This structural transition results in strain redistribution, contributing to the formation of the left peaks in the strain profile. On the other hand, the right peaks could correspond to the roller that applies a concentrated load to the ENF specimen.

The stiffness of the joint changes during each loading stage, causing variation in the strain behavior. For instance, prior to unstable crack propagation (from 0 to B), the left peaks gradually move to the right as the load increases. These left peaks reflect the changes occurring during the development of the FPZ. As the load further increases, the crack unstably propagates from B to C, and the two strain peaks merge into one, resulting in a single peak that potentially indicates the occurrence of unstable crack propagation. This will also be investigated through FE analysis in section 4.4. The strain peaks selected based on this approach are indicated by black crosses on the experimental curves of path C1-C2 in Fig. 10.

The crosses in Fig. 11 show the position of strain peaks captured by OBR along the path C1-C2, compared to the estimated lengths of other experimental techniques at

different stages. Similar to [13], the following analyses in this study do not consider DIC-SAZ based on horizontal displacement (dX); therefore, the term DIC-SAZ refers to the vertical displacement (dY) [13]. Apart from last stages, it is evident from the figure that the OBR strain peaks are constantly ahead of the lengths estimated by the other techniques. Previous studies have shown conflicting results regarding the ability of the strain peak captured from the specimen back-face to monitor the position of the crack tip. One study [18] found that it could identify the crack tip under both mode I and mode II loadings, while another [12] showed that it could detect the onset of the FPZ under mode I loading. To gain a better understanding of strain peaks' relationship with the crack tip position, in the case of mode II loading, it will be compared to the findings from the FE analysis presented in the following sections.

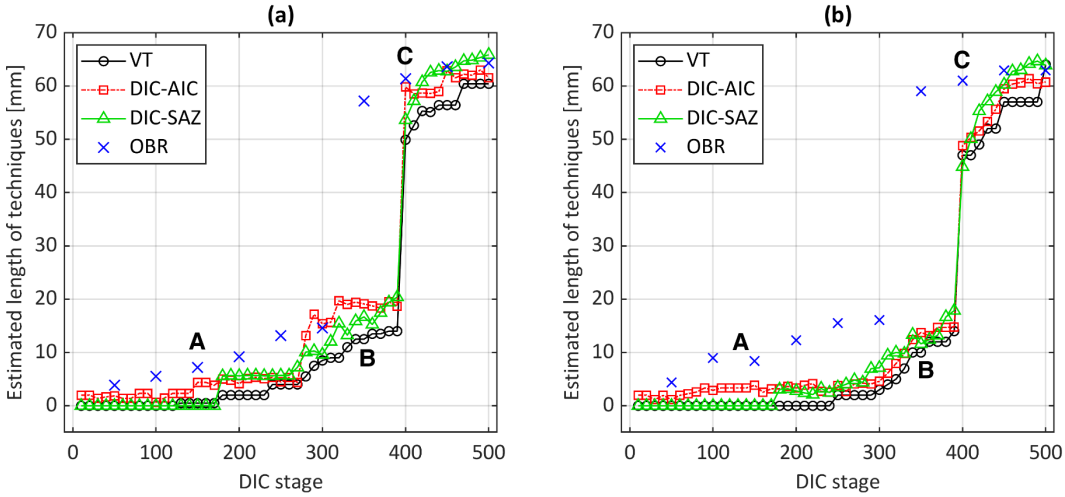

Fig. 11. Position of strain peaks captured by OBR in comparison to estimated crack length of other experimental techniques at different load levels for specimens (a) S1 and (b) S2.

4.3 Optimized cohesive parameters

The cohesive parameters (i.e., e_I, e_{II}, S_I and S_{II}) optimized for each specimen and TSL are listed in Table 3, while the corresponding trapezoidal and bi-linear TSLs are plotted in Fig. 12. Based on Table 3, both trapezoidal and bi-linear TSL appear to have a high e_I/e_{II} ratio. However, this does not necessarily imply that the material is stiffer in mode I loading than in mode II loading. The stiffness parameter (e) primarily plays a numerical role and does not reflect the actual material behaviour. In contrast, the low S_I/S_{II} ratio implies that the adhesive material has a higher stress bearing capability in mode II loading than in mode I loading. The most important parameters are G_{IC} and G_{IIC}, which reflect the actual fracture behavior of the adhesive under different loading conditions. In this

study, the G_{IC}/G_{IIC} ratio is less than 1, suggesting that more energy is required to propagate a crack in mode II loading than in mode I loading, which is crucial for understanding the mixed-mode fracture behavior of the adhesive.

Table 3. The optimized cohesive parameters obtained by Isight^{TM} software using bi-linear and trapezoidal TSLs for FE simulation of S1 and S2 samples. Note that the mode I critical toughness (G_{IC}) is adapted from [33].

Sample	TSL method	G_{IC} [N/mm]	G_{IIC} [N/mm]	S_I [MPa]	S_{II} [MPa]	e_I [MPa/mm]	e_{II} [MPa/mm]	R
S1	bi-linear	1.05	8.36	25	37.5	1,500	383	-
	trapezoidal	1.05	8.36	21.2	27.6	1,720	304	0.65
S2	bi-linear	1.05	7.64	28	39.5	1,811	402	-
	trapezoidal	1.05	7.64	28.3	24.5	2,207	371	0.6

The load-displacement curves of the optimized FE model, extracted using bi-linear and trapezoidal TSL, are compared to the experimental ones at different load levels for samples S1 and S2 in Fig. 13. Fig. 13 illustrates that the optimized bi-linear TSL was unable to closely match the experimental load-displacement curve, particularly beyond point B. In contrast, the trapezoidal TSL showed a better agreement with the experimental load-displacement curve.

While Cardamone et al.'s assessment [25] focused solely on comparing the experimental and numerical load-displacement curves, the current analysis goes a step further by considering the back-face strain profiles, as well. This approach provides a more comprehensive evaluation of the accuracy and reliability of each TSL, which will be further discussed in the following section.

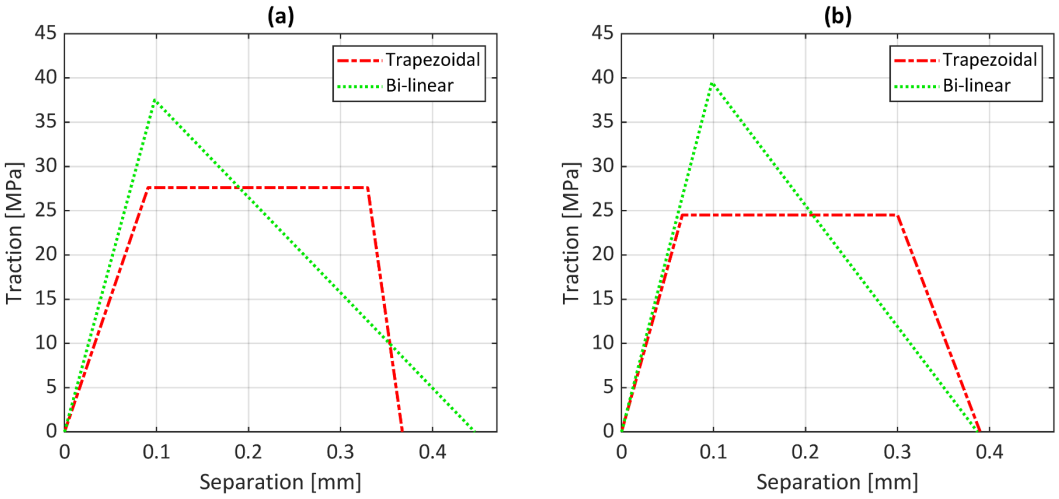

Fig. 12. Trapezoidal and bi-linear TSL shape obtained by the optimized cohesive parameters for samples (a) S1 and (b) S2.

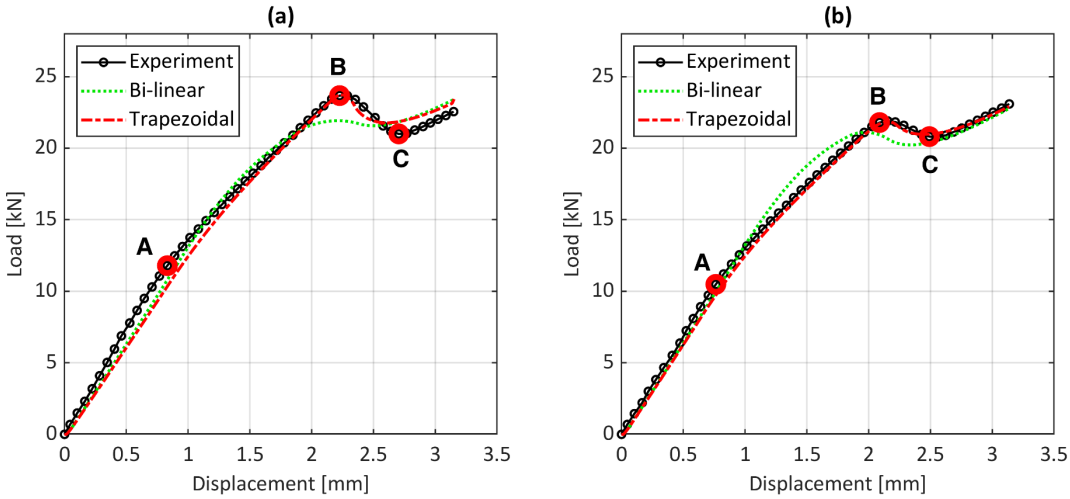

Fig. 13. The load-displacement curves of optimized FE model using bi-linear and trapezoidal TSLs in comparison to experiment for samples (a) S1 and (b) S2.

Moreover, a sensitivity analysis was conducted on the mode I and mode II cohesive parameters considering specimen #2 with a trapezoidal TSL. The dependency of the parameters was checked incrementally by adding and subtracting 25% and 50% of their optimal values. As shown in Fig. 14(a), it was found that the cohesive model is not overly dependent on mode I parameters including e_I and S_I. On the other hand, in Fig. 14(b), e_{II} notably affects the slope of the load-displacement curve, whereas S_{II} mostly influences the displacement at which failure occurs as shown in Fig. 14(c). Note that the trapezoidal TSL includes an additional plateau at the peak stress (see Fig. 12), which represents a phase where damage progresses at constant stress. This phase is followed by a steep decrease in traction, leading to a sharper drop at peak load (point B in Fig. 13) in the load-displacement curve. On the other hand, the bi-linear TSL assumes a linear behavior

between traction and separation and lacks such a plateau. As a result, it has a longer and less steep softening part, resulting in a smoother transition at peak load in the load-displacement curve. [26]

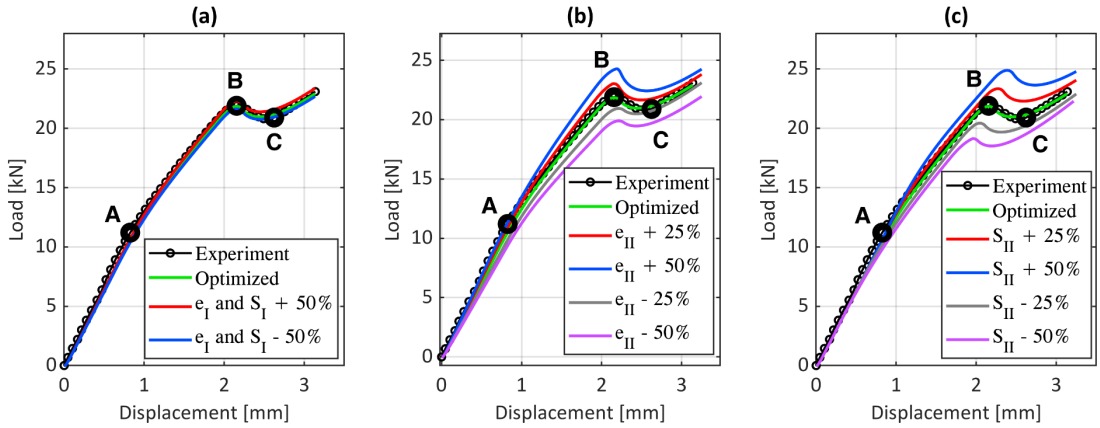

Fig. 14. The sensitivity check of mode I and mode II cohesive parameters: (a) e_I and S_I, (b) e_{II} and (c) S_{II}.

4.4 Bi-linear vs. trapezoidal TSL in crack propagation modelling

Since the FEM results in S1 are nearly identical to those in S2, only the results for S2 are discussed. As previously stated, in addition to the experimental and numerical load-displacement curves, the current analysis will take into account the back-face strain profiles for a more comprehensive comparison [25]. The load-displacement curve in the FEM is extracted from the loads and displacements of the upper roller. The back-face strain recorded by OBR is compared to the strain captured from the bottom edge of the specimen in the FEM (blue line in Fig. 4). Moreover, the state of the cohesive layer is described by the SDEG (scalar stiffness degradation) parameter. Once the SDEG value reaches 1, the cohesive element is considered as fully degraded and therefore it is eliminated, indicating the point at which a crack tip has fully developed. Black circles in Fig. 15 highlighted the location of this numerical crack tip. Cohesive elements with SDEG values greater than 0 and up to 0.999 constitute the fracture process zone [48,49].

The load-displacement curve and the back-face strain profile of the FEM extracted by bi-linear TSL in comparison to the experiment for different load levels are provided in Fig. 15. As observed previously, in Fig. 15 (a), it is evident that no bi-linear TSL could be optimized to effectively produce a load-displacement curve close to the experimental one beyond point B. More importantly, as shown in Fig. 15 (b), a discrepancy also exists in the strain profile recorded at the bottom edge of the FE model. Indeed, the numerical strain curves do not match well the trend or magnitude of the experimental ones.

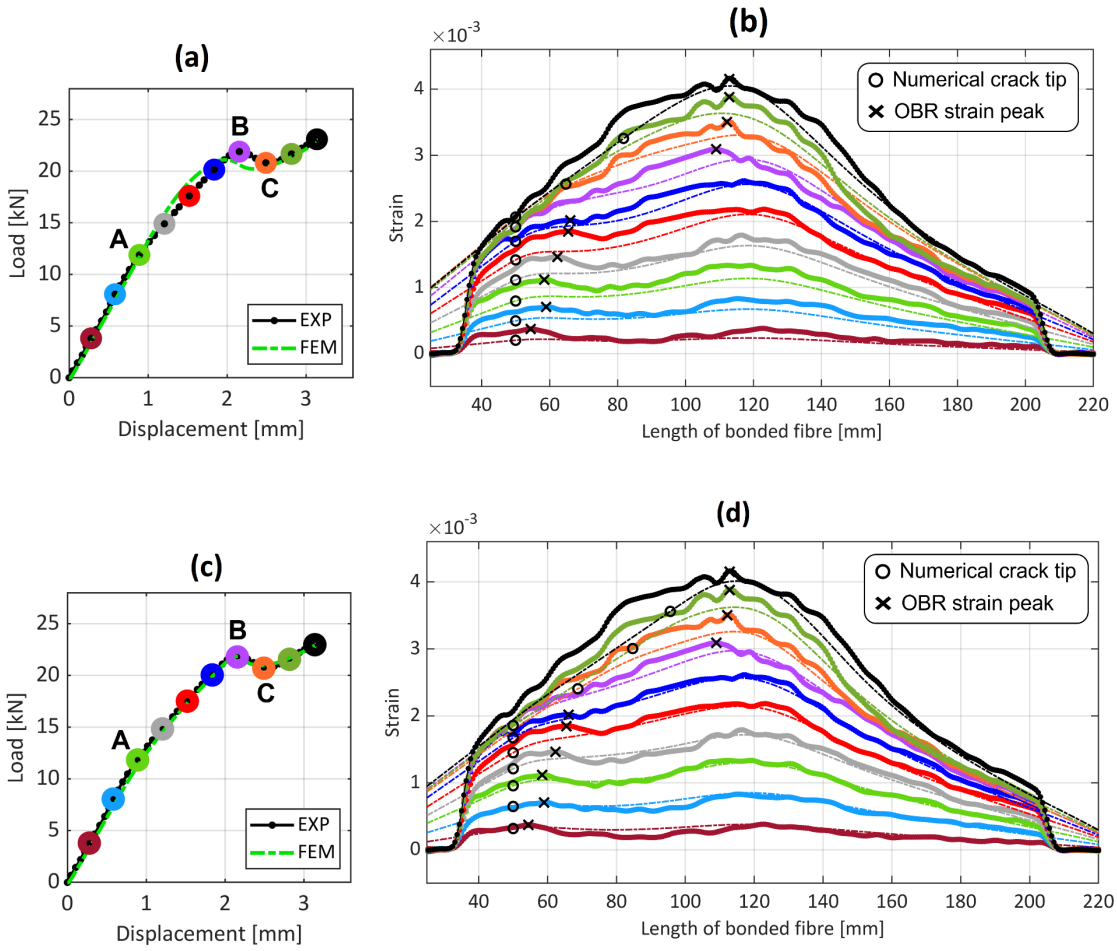

Fig. 15. Experimental load-displacement curve (solid curve) vs. FEM (dashed curve) for (a) bi-linear TSL and (c) trapezoidal TSL. Strain distribution recorded by OBR (solid curve) vs. FEM (dashed curve) corresponding to the given load-displacement curves for (b) bi-linear TSL and (d) trapezoidal TSL of sample S2.

On the other hand, it was possible to find a trapezoidal TSL through optimization which led to a good agreement with the full experimental load-displacement curve (see Fig. 15 (c)) and back-face strain profile (see Fig. 15 (d)). Before unstable crack propagation, both strain magnitude and the profile shape are in-line with the experimental ones. The agreement has been considerably improved with respect to the triangular TSL, although after crack propagation, the numerical strains were found to be lower than the experimental ones. However, even in these stages, the agreement is still better than the bi-linear TSL.

The poor agreement of the bi-linear TSL model in both load-displacement and back-face strain curves is likely due to the ductile behaviour of the adhesive, which is also reported in [33]. The trapezoidal TSL offers a better model for the elasto-plastic behaviour of the adhesive, as its shape (see Fig. 3 (b)) represents a longer damage softening than the

bi-linear TSL (see Fig. 3 (a)). For these reasons, in the following, the FE analysis was based on the trapezoidal TSL.

The FE analysis reveals that the OBR strain peak does not correspond to the position at which the crack has fully developed (SDEG = 1), i.e., the numerical crack tip. In Fig. 15 (d) for instance, prior to unstable crack propagation (from 0 to B), the peaks on the left are constantly ahead of the numerical crack tip, and gradually move to the right with increasing load. Even after unstable propagation, the position of the peaks remains ahead of the numerical ones. To better understand the meaning of the strain peaks detected by OBR, further FE analysis is employed in the following section. Such analysis can also help interpreting the position indicated by VT and DIC with respect to the numerical crack tip and the level of damage within the FPZ.

4.5 Comparison of the considered methods for crack length estimation

Fig. 16 shows that the FE model of the ENF sample corresponding to point C of the load-displacement curve. At this stage, some of the cohesive elements are fully damaged (SDEG = 1). The grey highlighted region in Fig. 16 represents the fully damaged zone, indicating the crack propagation in that area according to the simulation. Moreover, elements with SDEG greater than 0 and up to 0.999 are also highlighted ahead of the numerical crack tip. As shown, the FPZ thus seems to occupy a vast portion of the crack propagation region in the adhesive. This is consistent with both numerical and experimental analyses in the literature [13,25,49,50]. The FE analysis thus showed that a relatively small portion of the adhesive completely separated, while a significantly larger portion of it was damaged.

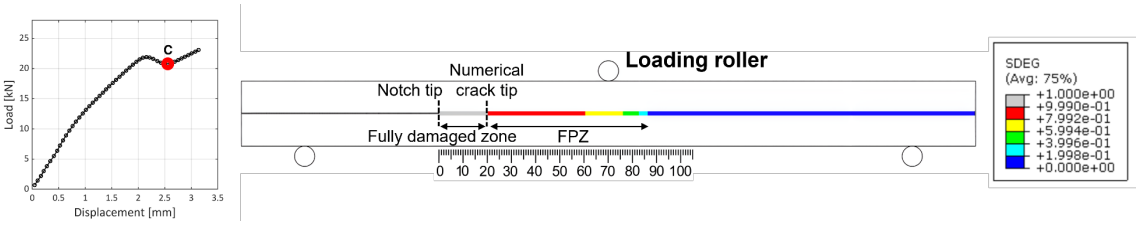

Fig. 16. The FE model of ENF sample under 20.8 kN load corresponding to point C on the load-displacement curve. The fully damaged zone contains the elements with SDEG = 1, while the FPZ includes all elements with 0 < SDEG ≤ 0.999.

Fig. 17 shows the location of the different analysed techniques over the bond line compared to the FE estimations. Before the load-displacement curve reaches point A, all

the techniques remain within 5 mm from the initial value reported for the first analysed stage (below 5 kN, Fig. 17 (a)). Interestingly, this initial value for the OBR was already about 5 mm ahead of the crack tip, while for the other techniques, the initial value was within 1.5 mm from the reference point at notch tip. At point A, the FE simulations highlight already in this stage the formation of a large FPZ (see Fig. 17 (c)). The OBR and the DIC-AIC seem to be slightly affected by such formation.

After point A and before reaching point B (see Fig. 17 (e)), the OBR moves by about 11 mm, while the other techniques did not vary significantly. According to the FE analysis, in these stages, the FPZ develops significantly. The consequent stress redistribution due to this development thus seems to affect the OBR more than the other techniques.

In point B (see Fig. 17 (g)), the FPZ keeps developing, with some elements already experiencing the softening part of the TSL (note that further FPZ development might have been prevented by the presence of the loading roller). In this point, the location identified by the OBR technique displayed a very large displacement, reaching a location close to the loading roller, possibly indicating the development of potential damage within the FPZ [13]. Moreover, the DIC-based techniques and the VT moved between 10 mm and 14 mm from the notch tip.

Finally, in the last analysed stages, corresponding to point C and beyond (see Fig. 17 (h), (i), and (j)), the DIC-based techniques displayed significant advancements, while the OBR remained close to the loading roller. Note that the DIC-based techniques and the VT seem to move together to very close locations.

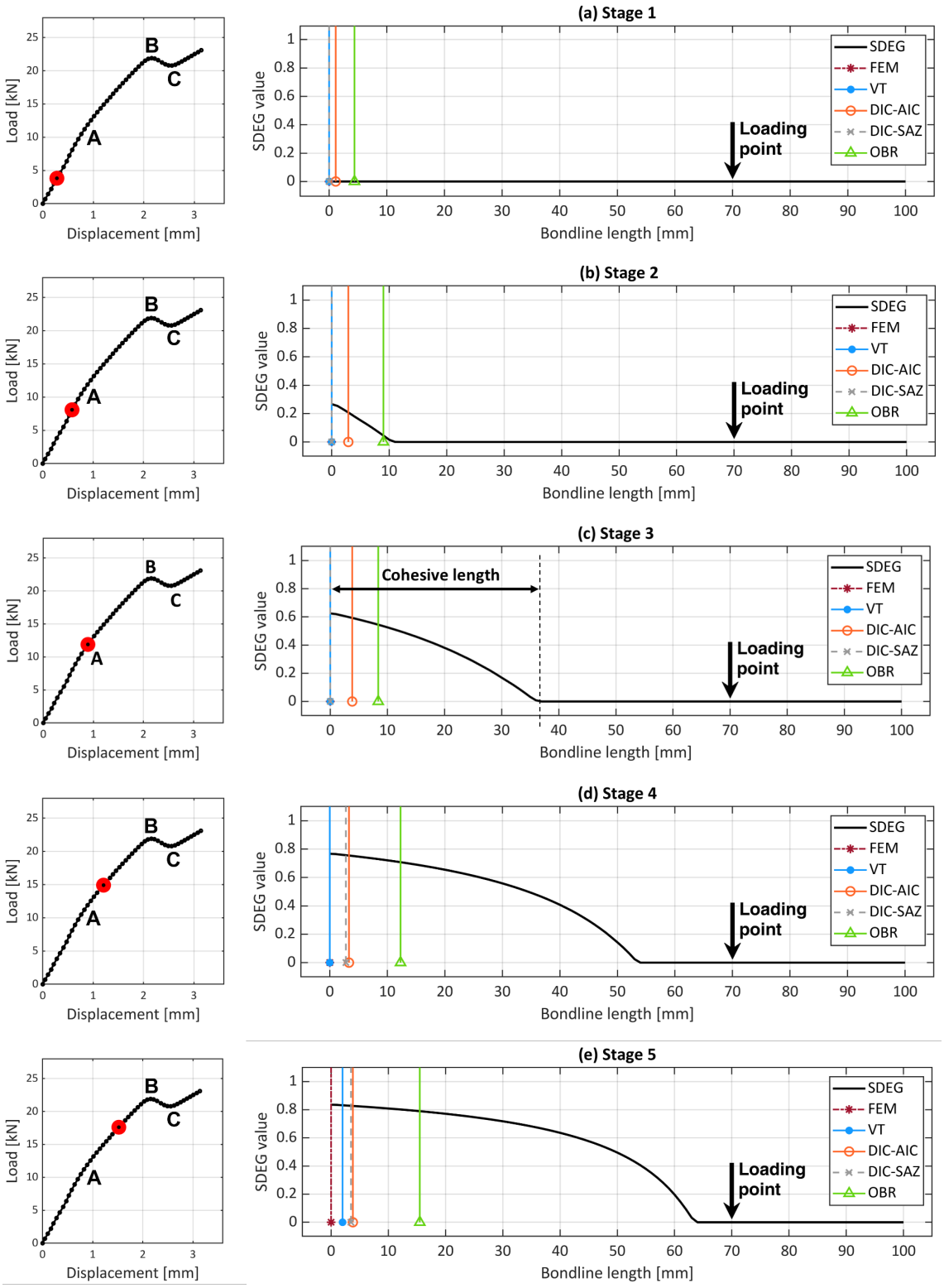
(a) Stage 1
(b) Stage 2
(c) Stage 3
(d) Stage 4
(e) Stage 5
Load [kN]
Displacement [mm]
A
B
C
SDEG value
Bondline length [mm]
Loading point
Cohesive length
SDEG
FEM
VT
DIC-AIC
DIC-SAZ
OBR

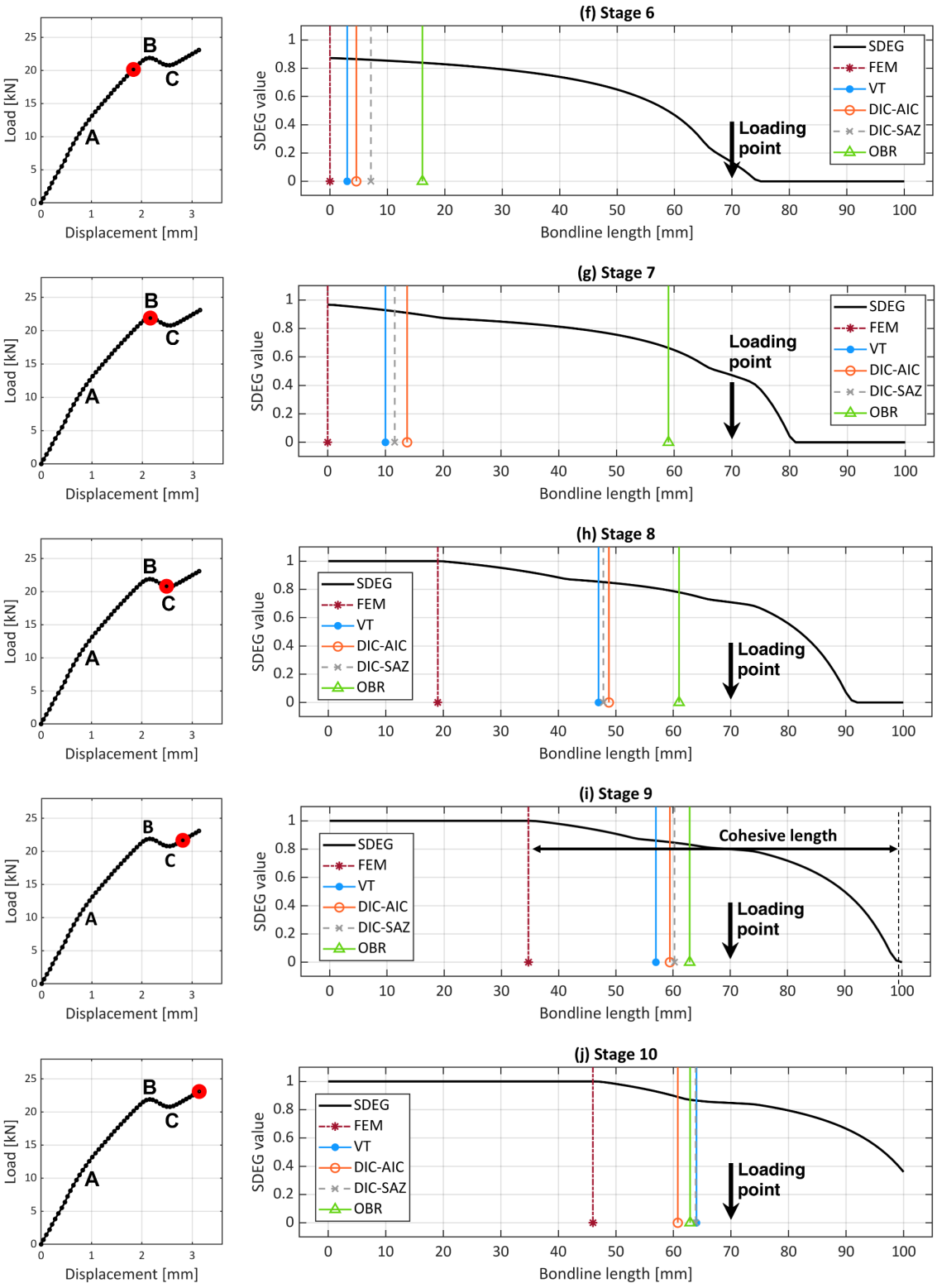

Fig. 17. Comparison of the estimated length of different techniques versus stiffness degradation (SDEG) of cohesive elements at different loading levels for specimen S2. The cohesive length is indicated by the black double arrow at (c) stage 3 and (i) stage 9.

From the above analysis, it is clear that the DIC-based techniques and the VT all identify very close points in the FPZ (ideally the same), while the OBR points out to a

different location further from the notch tip. It is arguable that the point identified by the three close techniques (DIC-AIC, DIC-SAZ and VT) might be the crack tip itself. This observation would be in contrast with the FE simulation, since this location does not correspond with the numerical crack tip. It is thus possible that the point identified by these techniques is ahead of the crack tip: indeed, the large process zone may cause earlier fracture in the paint for the VT, large displacements differences in the adherends for the DIC-based methods, or back-face strain redistribution for the OBR to justify an earlier detection. This last point could also be confirmed by the FE model: in the simulation, the distance between the identified point and the numerical crack tip is mostly composed of elements in the softening part of their TSL (see Fig. 17 (h) and (i)). The adhesive in this region is thus significantly more compliant (due to high damage) than the pristine adhesive, thus causing larger displacements and deformation.

5 Concluding remarks

This study employed experimental and numerical methods to estimate the crack length in metal-to-metal ENF adhesive joints under quasi-static mode II loading. Using OBR, the back-face distributed strain was measured. Additionally, a new strategy for crack length estimation based on adhesive shear strain using the DIC. Post-elaboration procedures were employed for OBR and DIC to estimate the crack tip position. The performance of these approaches was then compared to the VT and another DIC-based method developed by Orell et al. [13]. Finally, FE analysis was used to provide further insights into the interpretation of the positions detected by experimental techniques in relation to the numerical crack tip and the state of damage within the bondline, both before and after unstable propagation. The following conclusions were drawn based on the adhesive, loading conditions, and framework that were examined in this study.

- For the FE modelling of crack propagation, it was demonstrated that the trapezoidal TSL outperforms the bi-linear TSL, which was highlighted in both the load-displacement curve and the back-face strain profile.
- FE analysis revealed that a significant portion of the crack propagation region in the adhesive is occupied by the FPZ whereas only a relatively small portion of the adhesive experienced complete separation. The experimental methods appear to be influenced by this large FPZ and possible damage within it, with

OBR being more affected, and VT and DIC-based techniques being less affected.

- OBR back-face strain peak demonstrates its ability to detect potential damage within the adhesive that other methods may not capture, both before and after unstable propagation. This capability is especially advantageous for identifying early-stage damage in practical applications, such as crack initiation, before it progresses to complete failure.
- Both DIC-based techniques also show sensitivity in identifying a certain level of potential damage, which is less than OBR but similar to that of VT. This characteristic makes DIC valuable for detecting damage, both before and after unstable propagation.
- The VT is also consistent in identifying the significant level of possible damage within the bondline, similar to DIC-based techniques. Nevertheless, potential factors that may affect its performance must be considered, such as visual errors.

6 References

1 Kinloch, A. J. in *Adhesion and Adhesives: Science and Technology* (ed A. J. Kinloch) 188-263 (Springer Netherlands, 1987).

2 da Silva, L. F. M., Öchsner, A. & Adams, R. D. in *Handbook of Adhesion Technology* (eds Lucas F. M. da Silva, Andreas Öchsner, & Robert D. Adams) 1-7 (Springer International Publishing, 2018).

3 Richter-Trummer, V. *et al.* Analysis of crack growth behavior in a double cantilever beam adhesive fracture test by different digital image processing techniques. **42**, 452-459, doi:https://doi.org/10.1002/mawe.201100807 (2011).

4 Blaysat, B., Hoefnagels, J. P. M., Lubineau, G., Alfano, M. & Geers, M. G. D. Interface debonding characterization by image correlation integrated with Double Cantilever Beam kinematics. *International Journal of Solids and Structures* **55**, 79-91, doi:https://doi.org/10.1016/j.ijsolstr.2014.06.012 (2015).

5 Gorman, J. M. & Thouless, M. D. The use of digital-image correlation to investigate the cohesive zone in a double-cantilever beam, with comparisons to numerical and analytical models. *Journal of the Mechanics and Physics of Solids* **123**, 315-331, doi:https://doi.org/10.1016/j.jmps.2018.08.013 (2019).

6 Truong, H. T. X., Martinez, M. J., Ochoa, O. O. & Lagoudas, D. C. Mode I fracture toughness of hybrid co-cured Al-CFRP and NiTi-CFRP interfaces: An experimental and computational study. *Composites Part A: Applied Science and*

Manufacturing **135**, 105925, doi:https://doi.org/10.1016/j.compositesa.2020.105925 (2020).

7 Blackman, B. R. K., Kinloch, A. J., Rodriguez-Sanchez, F. S. & Teo, W. S. The fracture behaviour of adhesively-bonded composite joints: Effects of rate of test and mode of loading. *International Journal of Solids and Structures* **49**, 1434-1452, doi:https://doi.org/10.1016/j.ijsolstr.2012.02.022 (2012).

8 Azari, S., Papini, M., Schroeder, J. A. & Spelt, J. K. The effect of mode ratio and bond interface on the fatigue behavior of a highly-toughened epoxy. *Engineering Fracture Mechanics* **77**, 395-414, doi:https://doi.org/10.1016/j.engfracmech.2009.09.011 (2010).

9 de Castro, D. S. V. *et al.* Evaluation of Mode II Delamination Area by Non-destructive Techniques: Accuracy and Influence on Fracture Toughness Calculation. *Journal of Nondestructive Evaluation* **40**, 58, doi:10.1007/s10921-021-00789-3 (2021).

10 Vinciquerra, A. J. & Davidson, B. D. Effect of Crack Length Measurement Technique and Data Reduction Procedures on the Perceived Toughness from Four-Point Bend End-Notched Flexure Tests. **23**, 1051-1062, doi:10.1177/0731684404035413 (2004).

11 Meadows, L. *et al.* Distributed optical sensing in composite laminates. **52**, 410-421, doi:10.1177/0309324717723466 (2017).

12 Sourisseau, Q. *et al.* Use of high spatial resolution distributed optical fiber to monitor the crack propagation of an adhesively bonded joint during ENF and DCB tests. *International Journal of Adhesion and Adhesives* **115**, 103124, doi:https://doi.org/10.1016/j.ijadhadh.2022.103124 (2022).

13 Orell, O., Jokinen, J. & Kanerva, M. Use of DIC in the characterisation of mode II crack propagation in adhesive fatigue testing. *International Journal of Adhesion and Adhesives* **122**, 103332, doi:https://doi.org/10.1016/j.ijadhadh.2023.103332 (2023).

14 Wang, D., Ye, L., Tang, Y. & Lu, Y. Monitoring of delamination onset and growth during Mode I and Mode II interlaminar fracture tests using guided waves. *Composites Science and Technology* **72**, 145-151, doi:https://doi.org/10.1016/j.compscitech.2011.10.004 (2012).

15 Mohammadi, R., Ahmadi Najafabadi, M., Saghafi, H., Saeedifar, M. & Zarouchas, D. A quantitative assessment of the damage mechanisms of CFRP laminates interleaved by PA66 electrospun nanofibers using acoustic emission. *Composite Structures* **258**, 113395, doi:https://doi.org/10.1016/j.compstruct.2020.113395 (2021).

16 Sause, M. G. R. in *In Situ Monitoring of Fiber-Reinforced Composites: Theory, Basic Concepts, Methods, and Applications* (ed Markus G. R. Sause) 457-532 (Springer International Publishing, 2016).

17 Obaid, A. A., Yarlagadda, S., Yoon, M. K., Hager, N. E. & Domszy, R. C. A Time-domain Reflectometry Method for Automated Measurement of Crack Propagation in Composites during Mode I DCB Testing. **40**, 2047-2066, doi:10.1177/0021998306061309 (2006).

18 Lima, R. A. A., Perrone, R., Carboni, M. & Bernasconi, A. Experimental analysis of mode I crack propagation in adhesively bonded joints by optical backscatter reflectometry and comparison with digital image correlation. *Theoretical and Applied Fracture Mechanics* **116**, 103117, doi:https://doi.org/10.1016/j.tafmec.2021.103117 (2021).

19 Reiner, J., Torres, J. P. & Veidt, M. A novel Top Surface Analysis method for Mode I interface characterisation using Digital Image Correlation. *Engineering Fracture Mechanics* **173**, 107-117, doi:https://doi.org/10.1016/j.engfracmech.2016.12.022 (2017).

20 Rahman, S. A., Subhani, M. & Ashraf, M. Mode-II progressive fracture of sawn timber and timber-adhesive bond: experimental evaluation of end notched flexure (ENF) testing using DIC. *European Journal of Wood and Wood Products*, doi:10.1007/s00107-023-01968-x (2023).

21 Bernasconi, A. & Comolli, L. *An investigation of the crack propagation in a carbon fiber bonded joint using backface strain measurements with FBG sensors*. Vol. 8421 OFS (SPIE, 2012).

22 Kakei, A. A., Islam, M., Leng, J. & Epaarachchi, J. A. Use of an elasto-plastic model and strain measurements of embedded fibre Bragg grating sensors to detect Mode I delamination crack propagation in woven cloth (0/90) composite materials. **17**, 363-378, doi:10.1177/1475921717694812 (2018).

23 Sanderson, A. R., Ogin, S. L., Crocombe, A. D., Gower, M. R. L. & Lee, R. J. Use of a surface-mounted chirped fibre Bragg grating sensor to monitor delamination growth in a double-cantilever beam test. *Composites Science and Technology* **72**, 1121-1126, doi:https://doi.org/10.1016/j.compscitech.2012.01.022 (2012).

24 Güemes, A., Fernández-López, A. & Soller, B. Optical Fiber Distributed Sensing - Physical Principles and Applications. *Structural Health Monitoring* **9**, 233-245, doi:10.1177/1475921710365263 (2010).

25 Cardamone, S., Bernasconi, A. & Giglio, M. Characterization of the 3M Scotch-Weld™ 7260 B/A epoxy adhesive by cohesive damage models and application to a full-scale bonded sub-structure. *The Journal of Adhesion* **96**, 1270-1301, doi:10.1080/00218464.2019.1591278 (2020).

26 Akhavan-Safar, A., Marques, E. A. S., Carbas, R. J. C. & da Silva, L. F. M. in *Cohesive Zone Modelling for Fatigue Life Analysis of Adhesive Joints* (eds Alireza Akhavan-Safar, Eduardo A. S. Marques, Ricardo J. C. Carbas, & Lucas F. M. da Silva) 19-42 (Springer International Publishing, 2022).

27 Schwalbe, K.-H., Scheider, I. & Cornec, A. in *Guidelines for Applying Cohesive Models to the Damage Behaviour of Engineering Materials and Structures* (eds Karl-Heinz Schwalbe, Ingo Scheider, & Alfred Cornec) 17-31 (Springer Berlin Heidelberg, 2013).

28 da Silva, L. F. M. & Campilho, R. D. S. G. in *Advances in Numerical Modeling of Adhesive Joints* (eds Lucas Filipe Martins da Silva & Raul D. S. G. Campilho) 1-93 (Springer Berlin Heidelberg, 2012).

29 de Moura, M. F. S. F., Campilho, R. D. S. G. & Gonçalves, J. P. M. Pure mode II fracture characterization of composite bonded joints. *International Journal of*

Solids and Structures **46**, 1589-1595, doi:https://doi.org/10.1016/j.ijsolstr.2008.12.001 (2009).

30 Askarinejad, S., Martínez-Pañeda, E., Cuesta, I. I. & Fleck, N. Mode II fracture of an MMA adhesive layer: Theory versus experiment. *European Journal of Mechanics - A/Solids* **86**, 104133, doi:https://doi.org/10.1016/j.euromechsol.2020.104133 (2021).

31 Liu, R., Yu, Z. & Nasonov, F. Evaluations on VCCT and CZM methods of delamination propagation simulation for composite specimens. *Aerospace Systems*, doi:10.1007/s42401-023-00231-8 (2023).

32 Li, S., Thouless, M. D., Waas, A. M., Schroeder, J. A. & Zavattieri, P. D. Use of a cohesive-zone model to analyze the fracture of a fiber-reinforced polymer–matrix composite. *Composites Science and Technology* **65**, 537-549, doi:https://doi.org/10.1016/j.compscitech.2004.08.004 (2005).

33 Bernasconi, A. *et al.* Effect of temperature on cohesive modelling of 3M Scotch-Weld™ 7260 B/A epoxy adhesive. *The Journal of Adhesion* **96**, 437-460, doi:10.1080/00218464.2019.1665519 (2020).

34 Azevedo, J. C. S., Campilho, R. D. S. G., da Silva, F. J. G., Faneco, T. M. S. & Lopes, R. M. Cohesive law estimation of adhesive joints in mode II condition. *Theoretical and Applied Fracture Mechanics* **80**, 143-154, doi:https://doi.org/10.1016/j.tafmec.2015.09.007 (2015).

35 Jaillon, A., Jumel, J., Lachaud, F. & Paroissien, E. Mode I cohesive zone model parameters identification and comparison of measurement techniques based on uncertainty estimation. *International Journal of Solids and Structures* **191-192**, 577-587, doi:https://doi.org/10.1016/j.ijsolstr.2019.12.014 (2020).

36 Wang, Y., Williams, J. J. C. S. & Technology. Corrections for mode II fracture toughness specimens of composites materials. **43**, 251-256 (1992).

37 de Moura, M. F. S. F. & de Morais, A. B. Equivalent crack based analyses of ENF and ELS tests. *Engineering Fracture Mechanics* **75**, 2584-2596, doi:https://doi.org/10.1016/j.engfracmech.2007.03.005 (2008).

38 Rice, J. R. A Path Independent Integral and the Approximate Analysis of Strain Concentration by Notches and Cracks. *Journal of Applied Mechanics* **35**, 379-386, doi:10.1115/1.3601206 %J Journal of Applied Mechanics (1968).

39 Leffler, K., Alfredsson, K. S. & Stigh, U. Shear behaviour of adhesive layers. *International Journal of Solids and Structures* **44**, 530-545, doi:https://doi.org/10.1016/j.ijsolstr.2006.04.036 (2007).

40 Da Silva, L. F., Dillard, D. A., Blackman, B. & Adams, R. D. *Testing adhesive joints: best practices*. (John Wiley & Sons, 2012).

41 da Silva, L. F. M., de Magalhães, F. A. C. R. G., Chaves, F. J. P. & de Moura, M. F. S. F. Mode II Fracture Toughness of a Brittle and a Ductile Adhesive as a Function of the Adhesive Thickness. *The Journal of Adhesion* **86**, 891-905, doi:10.1080/00218464.2010.506155 (2010).

42 Fernández, M. V., de Moura, M. F. S. F., da Silva, L. F. M. & Marques, A. T. Characterization of composite bonded joints under pure mode II fatigue loading.

Composite Structures **95**, 222-226, doi:https://doi.org/10.1016/j.compstruct.2012.07.031 (2013).

43 Gonçalves, J. P. M., de Moura, M. F. S. F., de Castro, P. M. S. T. & Marques, A. T. Interface element including point-to-surface constraints for three-dimensional problems with damage propagation. *Engineering Computations* **17**, 28-47, doi:10.1108/02644400010308053 (2000).

44 Campilho, R. D. S. G., de Moura, M. F. S. F. & Domingues, J. J. M. S. Using a cohesive damage model to predict the tensile behaviour of CFRP single-strap repairs. *International Journal of Solids and Structures* **45**, 1497-1512, doi:https://doi.org/10.1016/j.ijsolstr.2007.10.003 (2008).

45 Brocks, W. in *Plasticity and Fracture* (ed Wolfgang Brocks) 151-170 (Springer International Publishing, 2018).

46 Akaike, H. A new look at the statistical model identification. *IEEE Transactions on Automatic Control* **19**, 716-723, doi:10.1109/TAC.1974.1100705 (1974).

47 Lima, R. A. A., Drobiazko, M., Bernasconi, A. & Carboni, M. On crack tip localisation in quasi-statically loaded, adhesively bonded double cantilever beam specimens by acoustic emission. *Theoretical and Applied Fracture Mechanics* **118**, 103286, doi:https://doi.org/10.1016/j.tafmec.2022.103286 (2022).

48 Stigh, U. *et al.* Some aspects of cohesive models and modelling with special application to strength of adhesive layers. *International Journal of Fracture* **165**, 149-162, doi:10.1007/s10704-010-9458-9 (2010).

49 Heshmati, M., Haghani, R., Al-Emrani, M. & André, A. On the strength prediction of adhesively bonded FRP-steel joints using cohesive zone modelling. *Theoretical and Applied Fracture Mechanics* **93**, 64-78, doi:https://doi.org/10.1016/j.tafmec.2017.06.022 (2018).

50 Sarrado, C., Turon, A., Costa, J. & Renart, J. An experimental analysis of the fracture behavior of composite bonded joints in terms of cohesive laws. *Composites Part A: Applied Science and Manufacturing* **90**, 234-242, doi:https://doi.org/10.1016/j.compositesa.2016.07.004 (2016).